ADVANCED SUSTAINABLE SYSTEMS
www.advsustainsys.com

Highly Active and Stable NiCuMo Electrocatalyst Supported on 304 Stainless Steel Porous Transport Layer for Hydrogen Evolution in Alkaline Water Electrolyzer

Andrea Zaffora, Francesco Di Franco, Davide Pupillo, Barbara Seminara, Giada Tranchida, and Monica Santamaria**

Several functionalized porous transport layers with Pt-free electrocatalysts for hydrogen evolution reaction in alkaline conditions, based on Ni, Cu, and Mo, are prepared through electrodeposition onto a 304 stainless steel mesh. Morphological characterization confirms the fabrication of electrodes with high electrochemical surface active area due to the formation of hierarchical nanostructures. Mo presence into the electrocatalysts increases the activity toward the hydrogen evolution reaction. The optimization of electrodeposition process leads to the preparation of highly active NiCuMo electrocatalyst that exhibits near zero onset overpotential and overpotentials of 15 and 113 mV at 10 and 100 mA cm^{-2}, respectively, in 1 M KOH electrolyte. Moreover, this electrocatalyst shows superior stability with respect to other Pt-free electrocatalysts, reaching 100 h of durability with low overpotentials value demonstrating the successful preparation of very promising functionalized porous transport layers for future-generation alkaline electrolyzers.

1. Introduction

Renewable energy storage became more and more critical in the path for a decarbonized society.[1–3] A way to store renewable electrical energy is producing fuels and chemicals that do not suffer of self-discharge phenomena. In this context, producing (and storing) green hydrogen is the key of the so called "hydrogen economy" and can be achieved through the electrochemical water-splitting process that produces hydrogen and oxygen at cathode and anode electrodes, respectively.[4–6]

Among the most mature technologies, alkaline electrolysis is already at commercial level, although it is still considered highly expensive with respect to classical hydrogen production processes based on fossil fuels.[4] Strategies for cost reduction can be implemented at three different levels: cell, stack, and system design. Stack costs (including porous transport layers (PTLs), bipolar plates, end plates, spacers etc.) can represent 40–50% of the total costs, thus it is necessary to reduce materials costs to further scale up alkaline electrolysis technology.

Currently, platinum group metals (PGM) and Co-based electrocatalysts are considered the best option for hydrogen evolution reaction (HER)[7,8] but designs without the employment of critical raw materials (CRMs)[9] are strongly desired. Moreover, electrodes with high specific surface area and new cell designs are continuously studied to increase the efficiency of the process. For instance, zero gap cell design is being studied to further increase the efficiency of alkaline water electrolysis by the reduction of the cell resistance contributions introducing a very small interelectrodic gap by using thin membranes or separators and porous electrodes rather than typical solid metal plates.[10] More specifically, catalyst-coated substrate (CCS) design can be thought to optimize cell design and minimize all the cell resistances. In this case, catalyst layer is directly deposited onto a porous substrate that acts, at the same time, as gas diffusion layer and effective electrode. At this aim, Ni mesh/foam can be used ensuring high specific surface area and an efficient gas management, allowing to the gas bubbles to detach soon from the electrode surface. Nevertheless, Ni substrates suffer of high cost that has been further increased due to the recent EU raw materials crisis. Therefore, the development of cost-effective and highly active CCS structure is needed to further scale up electrolyzer technology.

One of the best options to have cost-effective (i.e., PGM and CRMs free) and highly active catalyst for alkaline HER is developing high surface area Ni-based metal alloys.[11–13] Most active Ni-based electrocatalyst for HER under alkaline conditions is reported to be NiMo,[13] and different morphologies have been studied to increase the catalyst activity.[14,15] Moreover, also NiCu alloys have been found as promising metal alloys for HER, due to excellent stability, corrosion resistance, and efficiency.[16–19]

A. Zaffora, F. Di Franco, B. Seminara, G. Tranchida, M. Santamaria
Dipartimento di Ingegneria
Università degli Studi di Palermo
Viale delle Scienze, Ed. 6, 90128 Palermo, Italy
E-mail: francesco.difranco@unipa.it; monica.santamaria@unipa.it
D. Pupillo
Dipartimento di Scienza Applicata e Tecnologia
Politecnico di Torino
Corso Duca degli Abruzzi 24, 10129 Torino, Italy
The ORCID identification number(s) for the author(s) of this article can be found under https://doi.org/10.1002/adsu.202200486.

DOI: 10.1002/adsu.202200486

In particular, Cu-doped nanotubular Ni electrocatalyst was found to be highly active due, also, to the synergistic effect of Cu that, substituting to Ni sites in crystal structure, leads to an optimal ΔG^{H*} for hydrogen adsorption, therefore favoring H_2 desorption.[20]

Based on these findings, we developed high surface area NiCuMo electrocatalysts for HER with excellent activity and long-term durability. NiCuMo was deposited on a cheap 304 stainless steel (SS) mesh through an optimized one-step electrodeposition process in order to produce cost-effective and active CCS for zero-gap alkaline water electrolyzer. Electrodes were studied through morphological and chemical analysis carried out with SEM and EDX. Electrochemical characterization was carried out to have information about catalysts surface area and activity in 1 M KOH aqueous solution. Then, galvanostatic long-term durability test was performed in a flow-through cell.

2. Results and Discussion

NiCuMo electrocatalysts were fabricated by an electrodeposition process on a mesh made in AISI 304 SS, as described in the Experimental section.

The electrodeposition was conducted in an aqueous solution containing 0.5 M $NiSO_4$, 12.5 m_M $CuSO_4$, 0.5 M H_3BO_3, and a variable concentration of $(NH_4)_6Mo_7O_{24}$, from 7 mM to a concentration of 28 mM. Samples were then identified on the basis of the concentration of Mo-containing salt in the electrodeposition electrolyte, i.e., 0Mo is the sample obtained with no Mo in solution during the electrodeposition, 1Mo is the sample obtained with a 7 mM concentration of Mo salt arriving to 4Mo for the sample obtained with a 28 mM concentration. The electrolyte pH was corrected to 2.5 by the addition of H_2SO_4. The electrodeposition potential was set to –2 V (Ag/AgCl), so that Ni, Cu, and Mo are thermodynamically stable in their metallic state according to the following reactions and corresponding equilibrium potentials:[21]

$$Ni^{2+} + 2e^- \rightarrow Ni \quad E_{eq} = -0.25 + 0.0295 \log\left[Ni^{2+}\right] \text{V SHE} \tag{1}$$

$$Cu^{2+} + 2e^- \rightarrow Cu \quad E_{eq} = 0.337 + 0.0295 \log\left[Cu^{2+}\right] \text{V SHE} \tag{2}$$

$$Mo^{3+} + 3e^- \rightarrow Mo \quad E_{eq} = -0.20 + 0.0197 \log\left[Mo^{3+}\right] \text{V SHE} \tag{3}$$

During the electrodeposition process, a cathodic current slightly increasing with time was recorded for all the investigated bath composition (see Figure S1, Supporting Information).

After the electrodeposition process, it was important to estimate the roughness factor of the NiCuMo electrodes to assess the electrochemically active surface area (ECSA). At this aim, we recorded EIS spectra in 1 M KOH in O_2-free environment at 0.15 V RHE to hinder the possible O_2 reduction process, thus having only capacitive current relating to the double layer capacitance (C_{DL}). Indeed, at this electrode potential, water reduction reaction is not thermodynamically possible. EIS spectra related to all the electrodes produced by electrodeposition process are shown in **Figure 1**a) in Nyquist representation. For comparison, EIS spectra of not functionalized 304 SS mesh and 0Mo electrode are reported in Figure S2 (Supporting Information).

EIS spectra were fitted with the equivalent electrical circuit reported in the inset of Figure 1b), i.e., a series between R_s, the electrolyte resistance, and a parallel between R_{CT}, a resistance to model the charge transfer resistance, and $Q_{DL,el}$, a constant-phase element (CPE) modeling the nonideal electrode double layer capacitance. The electrode double layer capacitance, $C_{DL,el}$, is derived from $Q_{DL,el}$ by the following equation:[22]

$$C_{DL,el} = Q_{DL,el}^{1/n} \, R_s^{(1-n)/n} \tag{4}$$

Fitting parameters (see Table S1, Supporting Information) clearly show a significant reduction of charge transfer resistance and a relevant increase of the double layer capacitance after the electrodeposition process that can be explained by the enhanced roughness (and thus active area) of the coated electrodes. Assuming a double layer capacitance of 50 µF cm^{-2} (as that measured using a flat mirror-finished AISI 304 coupon), the roughness factor r was estimated according to the following equation:

$$r = \frac{C_{DL,el}}{50\ \mu F\ cm^{-2}} \tag{5}$$

r values are reported in **Table 1** for all the electrodes.

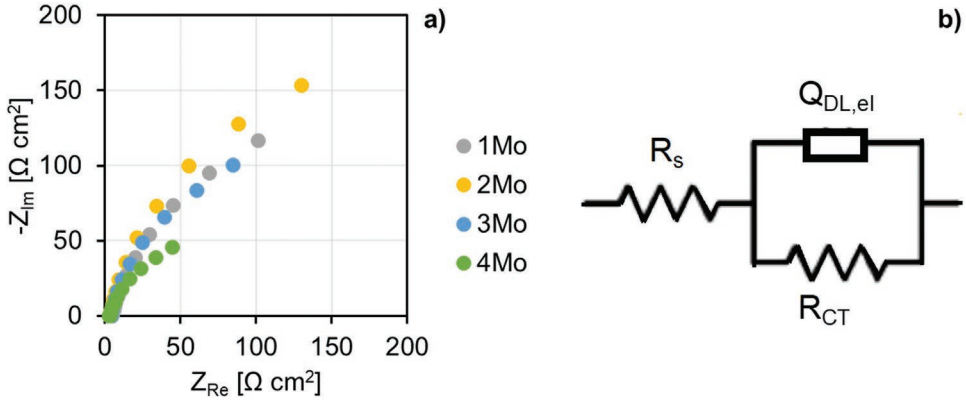

Figure 1. a) EIS spectra, reported in Nyquist representation, recorded at 0.15 V RHE related to all the Mo-containing electrodes. b) Equivalent electrical circuit used for fitting EIS spectra.

Table 1. Roughness factor of all the electrodes produced by the electrodeposition process.

	Bare 304 SS mesh	NiCu (0Mo) electrode	1Mo electrode	2Mo electrode	3Mo electrode	4Mo electrode
Roughness factor, *r*	4	15	71	44	75	164
Ni Cu Mo NiMo CuMo	Ni	Cu	Mo	NiMo	CuMo	
Roughness factor, *r*	2	57	3	2	77	

Bare 304 SS mesh has a *r* of ≈4, while coated electrodes have *r* values increasing with an increased concentration of Mo salt in the solution, ranging between 71 for 1Mo sample and 164 for 4Mo sample. Therefore, tailoring the electrodeposition process, it is possible to obtain electrodes with an increased ECSA, necessary to have high activity for HER reaction. However, the roughness factors reported in Table 1 can only in part explain the huge differences in the R_{CT} estimated by the fitting procedure. Indeed, the charge transfer resistance for the 304 SS mesh is very high (3×10^4 Ω cm^2) as expected for an ideally polarizable interface, and two order of magnitude higher than that estimated for coated electrodes. The very low charge transfer resistance can be explained considering that at this potential a Faradaic process can occur (namely Mo oxidation in agreement with the thermodynamic predictions of Molybdenum Pourbaix diagram).

Based on catalyst mass loadings estimated from mass differences before and after the electrodeposition process (see Figure S3, Supporting Information), it is possible to obtain high specific surface area values ranging between 3 m^2 g^{-1} for 1Mo sample to 11 m^2 g^{-1} for 4Mo sample.

SEM images, related to 0Mo and 3Mo electrodes, are shown in **Figure 2**a–d), while for 1Mo, 2Mo, and 4Mo electrodes, SEM micrographs are reported in Figure S4 (Supporting Information). In the case of electrodeposition without Mo ions in solution (0Mo sample), NiCu coating is not uniform throughout the 304 SS mesh substrate and it presents agglomerates with needle-shaped tips. This leads to a not high roughness factor (see Table 1), only ≈four times higher than that estimated for 304 SS mesh sample. The presence of MoO_4^{2-} ions in the electrodeposition bath (see Figure 2c,d and Figure S4, Supporting Information) leads to higher roughness factors due to more

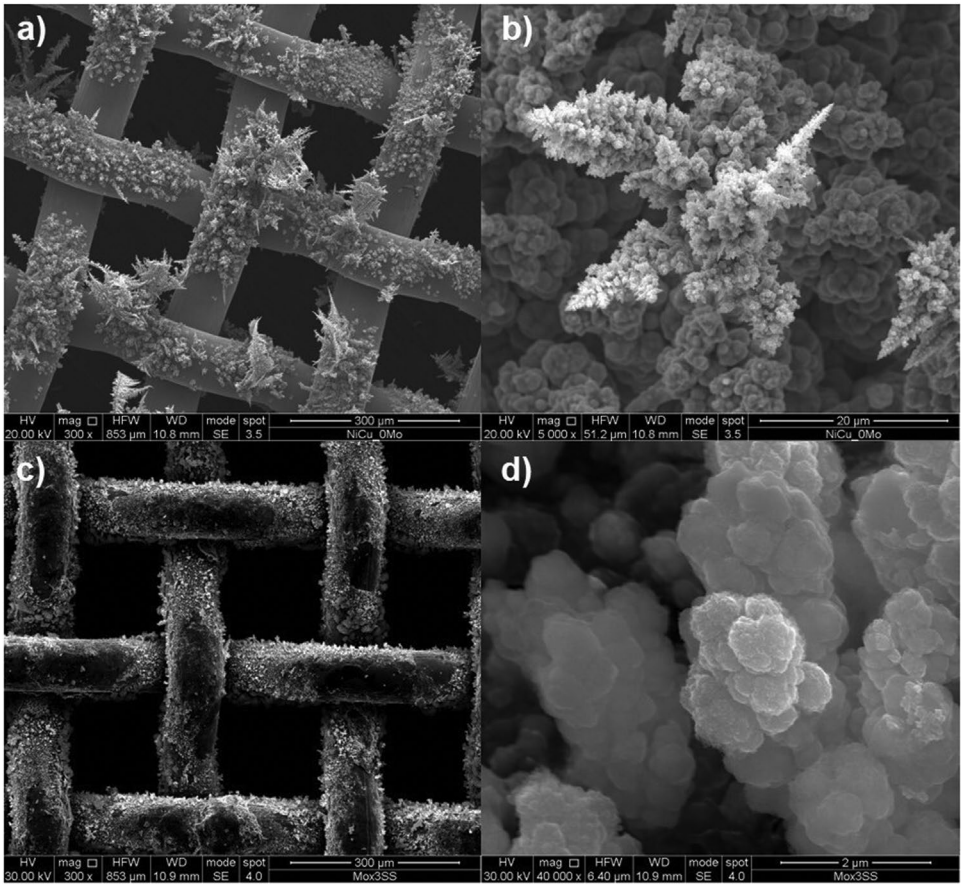

Figure 2. SEM images of 0Mo (NiCu) electrode at: a) low magnification and at: b) high magnification and of 3Mo electrode at: c) low magnification and at: d) high magnification.

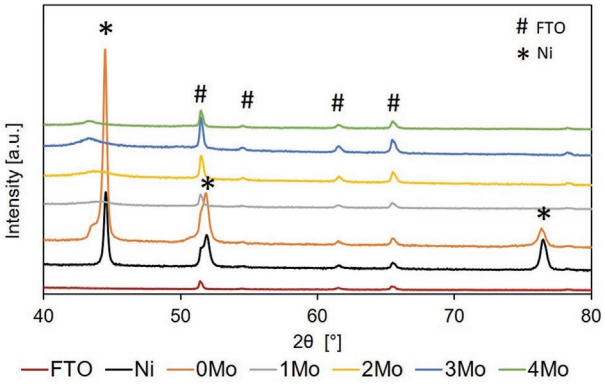

Figure 3. XRD patterns of the electrodeposited samples on FTO.

ordered nanostructure. In fact, in the case of 3Mo electrode, after the electrodeposition process, the 304 SS mesh surface is totally covered with particles with average diameter of ≈600 nm, organized in hierarchical structures (see Figure 2d). Same hierarchical structures can be observed for 1Mo, 2Mo, and 4Mo electrodes (see Figure S4, Supporting Information).

The crystal structures of the electrodeposited samples were characterized by XRD. As shown in **Figure 3**, the XRD patterns for Ni and 0Mo are crystalline with three main reflections at $2\theta = 44.44°$, 51.26°, and 76.35°, corresponding to (111), (200), and (220) planes of face-centered cubic Ni. For 0Mo, the shoulder peaks appear at the base of Ni (111) and (200), indicating the partial formation of NiCu alloy.[23] This result suggests that partial replacement of Ni with Cu leads to an expansion of pure Ni lattice, as Cu has larger lattice parameter (i.e., 0.362 nm) than that related to Ni structure (i.e., 0.350 nm), therefore in agreement with the alloy formation. Several papers report such experimental findings during co-electrodeposition of Ni and Cu.[24–26] When the Cu content is higher than almost 50%, there can be segregation of the individual atoms rather than the formation of a homogeneous alloy.[25] It is worth noting the effect of Mo presence on the crystallinity degree of Ni. The characteristic Ni peaks disappeared in the Mo-containing Ni sample, suggesting a highly disordered structure. Moreover, no characteristic peaks corresponding to Mo or NiMo are present, indicating that Mo atoms are dissolved into the lattice of Ni. For NiCuMo samples, a small and broad peak at ≈43.5° was observed, which suggests the poor crystallization of metallic Ni coating, as well as that a portion of Ni crystalline structures were kept in spite Mo deposition.[27] The XRD diffraction peak of the NiMo alloy should have a small shift relative to the pure Ni coating[27] but, in the case of NiCuMo alloys, it overlaps to NiCu diffraction peak. All these experimental findings suggest that solid solution of Cu and Mo in Ni is formed in the exploited composition range.

Figure 4 shows the XPS Cu 2p, Mo 3d, and Ni 2p core level spectra. In Figure 4a, the Cu 2p core level spectra exhibit peaks at 932.5 eV related to Cu^0, 933.8 and 934.5 eV related to Cu^{2+}. Another peak corresponding to Cu^{2+} were observed at higher binding energy close to 954 eV.[28–30]

For Ni 2p core level spectra (Figure 4b), three peaks are detected: peak at 852.9 eV related to Ni^0 while peaks at 856 and 861 eV are related to Ni^{2+}.[31–33] Mo 3d core level spectra (Figure 4c) show two peaks at 232.6 and 235.7 eV, both related to Mo^{6+} species.[31] In **Table 2**, the atomic compositions obtained by XPS fitting are reported.

XPS characterization reveals the presence of oxidized species for Cu, Ni, and Mo on the samples, while XRD characterization detects patterns diffraction related to only metallic species. This could be explained by considering that XRD is a bulk technique while XPS is a surface technique and thus it is able to detect thin-air-formed passive films on metallic substrates. Moreover, when the electrode works as cathode for the hydrogen evolution process, it is likely that these species are also reduced due to the very negative working potential, thus cancelling the effect of air exposure.

Electrocatalytic performance of NiCuMo electrodes was evaluated by electrochemical measurements, more specifically galvanodynamic and electrochemical impedance spectroscopy measurements.

Galvanodynamic measurements (with 95% iR drop correction) carried out in 1 M KOH aqueous solution are reported in

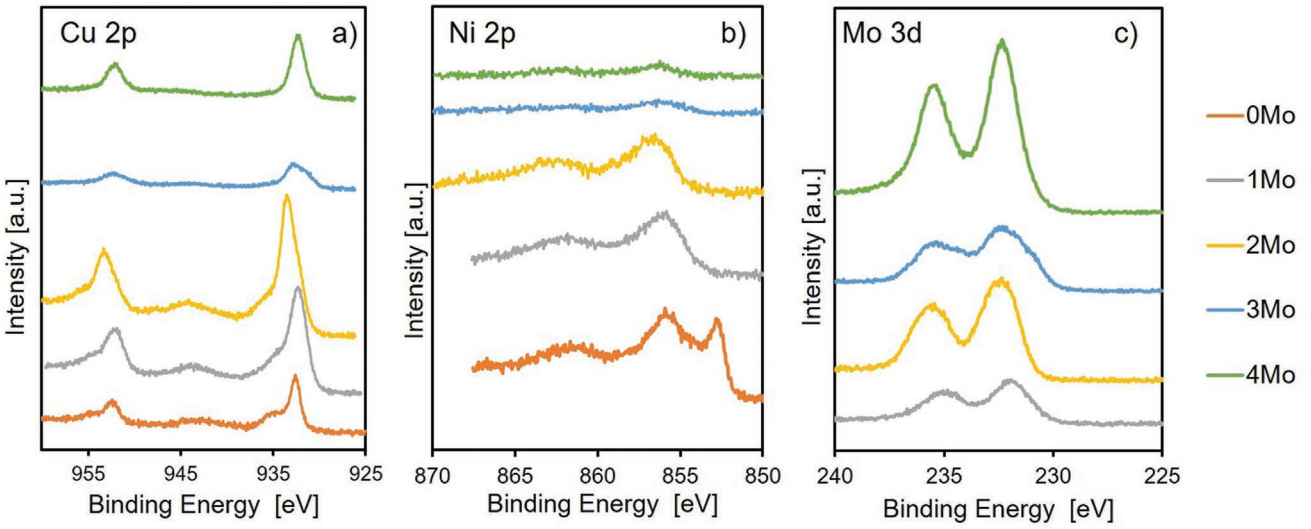

Figure 4. XPS: a) Cu 2p, b) Ni 2p, and c) Mo 3d high-resolution core level spectra for all the Mo-containing electrodes.

Table 2. Atomic compositions of all the Mo-containing electrodes obtained by XPS.

Sample	O [at%]	Ni [at%]	Cu [at%]	Mo [at%]
0 Mo	61.7	23.1	–15.2	–
1 Mo	70.3	11	15.1	3.6
2 Mo	69.1	6.8	17.2	6.9
3 Mo	74.6	3.8	7.7	13.9
4 Mo	71.8	3.0	8.3	16.9

Figure 5a) for 304 SS mesh soon after chemical etching as well as for 304 SS mesh after electrodeposition in electrolyte with different molybdate concentration. Current density is normalized for surface geometric area of electrode immersed in KOH solution.

It is immediately noticeable that the presence of Mo in the electrodes plays a crucial role, greatly improving the electrocatalytic performance. In fact, 304 mesh and NiCu sample (i.e., 0Mo electrode) display an onset overpotential for HER of 300 and 70 mV, respectively. The presence of Mo, regardless of Mo salt concentration during the electrodeposition process, leads to an onset overpotential for HER close to 0 mV. This result highlights that a high surface area is not sufficient to obtain highly active electrocatalysts but it even more important the chemical composition of the catalyst surface. By looking at η_{10} and η_{100} values (reported in Figure 5b), it can be seen that 3Mo sample is the best electrode with respect to electrocatalytic performance. η_{10} and η_{100} values of 443 and 577 mV, respectively, were estimated for bare 304 SS mesh, while η_{10} and η_{100} values of 302 and 486 mV, respectively, were estimated for the electrode not containing Mo. Optimizing Mo ions concentration during the electrodeposition process led to obtain an electrode with highly performing characteristics, in fact, very small η_{10} and η_{100} values of 15 and 113 mV, respectively, were estimated for 3Mo electrode. η_{10} value is currently one of most reported benchmarks for the activity of an electrocatalyst and it is related to the potential at –10 mA cm^{-2} corresponding, for a photoassisted water-splitting process, to a solar-to-hydrogen efficiency of 12.3% (i.e., the required efficiency for cost-competitive solar water splitting).[34] The value obtained for 3Mo electrode is close to the lowest ever-reported η_{10} value for heterostructures electrocatalysts for HER in alkaline solutions.[20,35–36] This result is outstanding, considering also that 3Mo electrode is obtained in a one-step electrodeposition process using a very cheap 304 SS mesh as PTL.

Figure 5c shows linear portions of the Tafel plot (overpotential η vs log(i) related to the curves reported in Figure 5a) for all the synthesized electrocatalysts. Linear part of Tafel plot can be fitted according to the following equation:

$$\eta = a + b \times \log(\mathrm{i}) \tag{6}$$

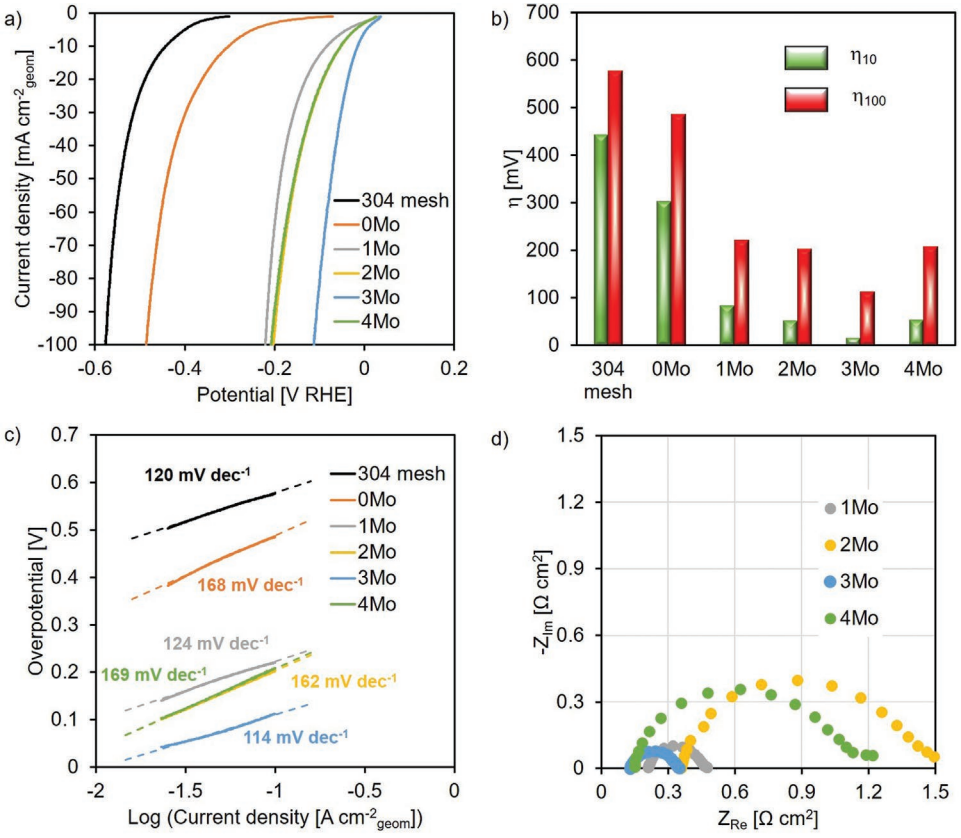

Figure 5. a) Current density versus electrode potential curves related to all the electrodes, recorded in 1 M KOH aqueous solution. b) Overpotential values estimated at –10 and –100 mA cm^{-2} for all the electrodes. c) Tafel slopes values. d) EIS spectra, reported in Nyquist representation, recorded at –0.15 V RHE related to all the Mo-containing electrodes.

Table 3. Exchange current density values for all the electrodes produced by the electrodeposition process.

	Bare 304 SS mesh	NiCu (0Mo) electrode	1Mo electrode	2Mo electrode	3Mo electrode	4Mo electrode
Exchange current density, i_0 [A cm^{-2}_{real}]	4.1×10^{-7}	8.5×10^{-6}	2.3×10^{-5}	1.2×10^{-4}	1.5×10^{-4}	3.6×10^{-5}
Ni Cu Mo NiMo CuMo	Ni	Cu	Mo	NiMo	CuMo	
Exchange current density, i_0 [A cm^{-2}_{real}]	5.7×10^{-5}	4.1×10^{-7}	1.7×10^{-6}	2.9×10^{-3}	1.5×10^{-6}	

where a is directly proportional to the logarithm of the exchange current density that is a measure of the inherent electrocatalytic properties of the material, and b is called Tafel slope that is another important kinetic parameter, and it is related to the reaction mechanism. The exchange current density, i_0, is significantly affected by the composition of the catalytic layer and, to cancel the contribution due to the different roughness factors on i_0, the latter were normalized for r (see **Table 3**). The results show that the coating deposited from 3Mo has the best i_0 and k_0, i.e. the standard rate constant.

Estimated Tafel slope values are reported in Figure 5c. The lower is b, the better is the electrocatalytic performance of the electrode. The lowest Tafel slope (114 mV dec^{-1}) was assessed for 3Mo electrode, confirming the best electrocatalytic performance for this electrode. This Tafel slope value is compatible with a reaction mechanism that foresees the Volmer reaction (i.e., water molecule reacts with an electron on the electrode surface to generate an adsorbed H* atom) as rate-determining step of HER process.[13,34]

EIS spectra, recorded at –0.15 V RHE, are shown Figure 5d in Nyquist representation. EIS spectra were fitted according to the equivalent electrical circuit reported in Figure 1b. Fitting parameters are reported in Table S2 (Supporting Information) for all the electrodes. As it is possible to note, the lowest R_{CT} value (0.21 Ω cm^2) was found for 3Mo electrode, in agreement with the lowest overpotential recorded for this electrode with respect to the other electrodes synthesized for this work. The presence of Mo into the electrocatalyst can facilitate the kinetics of water adsorption,[37] i.e., of the first step of HER in alkaline medium, therefore having a synergistic action with Ni and Cu, which facilitate hydrogen desorption for the surface, leading to very high catalytic activity.

In order to understand the effect of single elements, therefore of the layer composition, on the performance toward HER, we recorded current density versus potential curves also for electrodeposited Ni, Cu, Mo, NiMo, CuMo samples to have a complete view of the catalysts effect (see Figure S5, Supporting Information). Ni, Cu, Mo, and CuMo samples have worse performance toward hydrogen evolution reaction, in terms of η_{10} and η_{100} values with respect to the best NiCuMo alloy. This is due to lower exchange current density values corrected for the roughness factor estimated by the procedure described in the manuscript. In Tables 1 and 3 are also reported roughness factor values and exchange current density values, respectively, for the Ni, Cu, Mo, Ni-Mo, and Cu-Mo samples.

It is possible to note the effect of Cu addition in increasing the real-active surface area, as also confirmed by SEM images reported in the Supporting Information file for Cu and CuMo samples (see Figures S7 and S9, Supporting Information). It is worth noting that, in the case of NiMo sample, the roughness factor remains low, due to the absence of Cu, but the electrocatalytic activity (i.e., real i_0, see Table 3) is higher than any other sample. Anyway, the performance is lower than best NiCuMo alloy, highlighting that the composition of the layer plays a key role. Indeed, H-adsorption on Cu-doped Ni(111) is weaker than in the case of Ni with consequent enhancement of HER activity as reported in the literature[20,23] and as confirmed by the experimental results of this work.

It is very well known that the interaction between H atom and catalyst surface should be neither too weak, to correctly adsorb reactants, nor too strong, to efficiently release produced hydrogen. The presence of two empty d-orbitals in Ni, useful for H atom adsorption/desorption, can efficiently promote electron transfer and H–O bond breakage. According to Brewer Engel valence bond theory, the electron density of transition metals with more-filled d orbitals, as Ni, can be modified when alloyed to metals as Mo with empty or half-filled d-orbitals, that in turn facilitate M-H_{ads} formation.[38] The presence of both Cu (i.e., a M-H bond weakener) and Mo (i.e., M-H bond strengthener) allows a good compromise with consequent enhancement of the catalytic activity.

Another crucial criterion for the practical application of these electrocatalysts is the electrochemical stability, i.e., a constant overpotential for HER with operating time, sign of a stable electrochemical activity of the electrode. Chronopotentiometric curve of 3Mo electrode recorded at –100 mA cm^{-2} in 1 M KOH is shown in **Figure 6**a.

After a transitory of ≈1 h, the overpotential for HER remains quite stable for (at least) 100 h, with a value of 165 ± 45 mV, demonstrating the high stability of this electrode. This is the lowest overpotential value if compared with other values reported in the literature for stability tests carried out at 100 mA cm^{-2} for 100 h.[23,39]

To further demonstrate the outstanding stability of 3Mo electrocatalyst, the electrode was studied after the stability test with morphological characterization and evaluating Ni, Cu, and/or Mo loss during 100 h polarization by ICP-OES.

By ICP-OES analysis, Ni and Cu ions were not detected in the electrolyte samples collected during the stability test. This result can be explained by considering that, during shutdown times, Ni and Cu are thermodynamically stable in 1 M KOH aqueous solution while, during operating time, they are cathodically protected operating in immunity zone of corresponding Pourbaix diagrams.[21] Regarding Mo, a certain concentration of Mo species in the electrolyte during the stability test was detected. In fact, both during shutdown and operating times, Mo can dissolve according to the following reaction:[21]

$$\begin{aligned} &Mo + 4H_2O \rightarrow MoO_4^{2-} + 8H^+ + 6e^- \\ &E_{eq} = 0.154 - -0.078\,pH + 0.01\log\left[MoO_4^{2-}\right] V\,SHE \end{aligned} \quad (7)$$

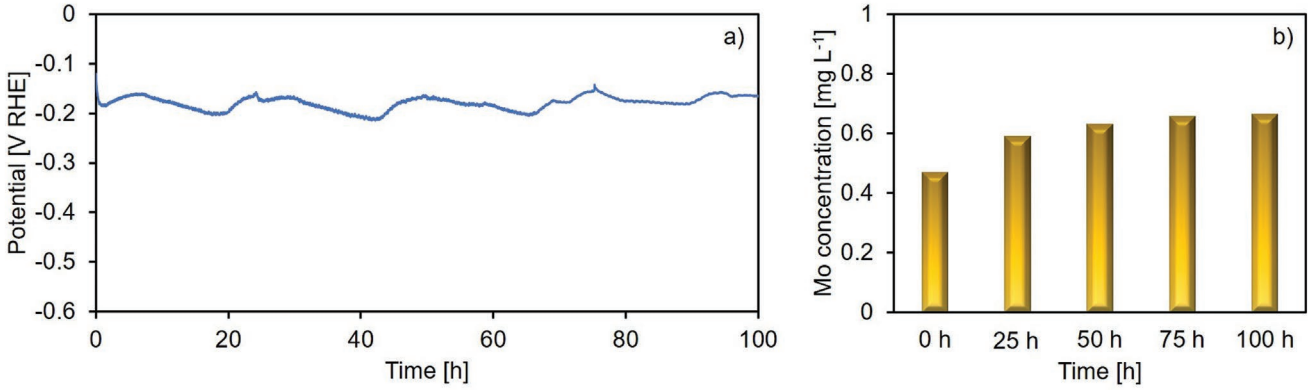

Figure 6. a) The stability test for 3Mo electrode carried out at –100 mA cm^{-2} for 100 h. b) Mo concentration in the electrolyte at different times during the stability test.

Anyway, concentration of Mo ions in the electrolyte keeps really low values during stability tests, from 0.469 mg L^{-1} at 0 h to 0.664 mg L^{-1} at the end of stability test (see Figure 6b), corresponding to a dissolution rate equal to 40 nmol cm^{-2} h^{-1}, further demonstrating the high stability of the electrode during operation time.

SEM images and catalyst composition reported in **Figure 7** were obtained after 100 h stability test.

Average particles diameter is ≈1.3 µm, i.e., average diameter value doubled after the stability test indicating the loss of ECSA. At the same time, chemical composition indicates Mo loss during 100 h polarization test. However, HER overpotential and R_{CT} values remained almost unchanged during the stability test, indicating a preserved electrochemical activity of the catalyst.

3. Conclusions

We optimized an electrodeposition process to produce Pt-free and CRM-free NiCuMo electrocatalyst, supported by a 304 SS mesh, for HER reaction showing high catalytic activity and high stability. Electrocatalysts' high electrochemical surface active area was assessed by electrochemical measurements and by SEM and it is due to hierarchical nanostructures. Best η_{10} and η_{100} values of 15 and 113 mV, respectively, were estimated that are lower of most of the Pt-free and CRM-free state-of-art electrocatalysts for HER. Furthermore, outstanding stability was demonstrated, i.e., 100 h at –100 mA cm^{-2} with an overpotential value of 165 ± 45 mV, with neglecting Ni and Cu dissolution and low dissolution rate for Mo during operating conditions. The combination of Ni and Cu with Mo led to very active electrocatalyst, demonstrating the successful preparation of very promising functionalized porous transport layers for future-generation alkaline electrolyzers.

4. Experimental Section

Preparation of Stainless Steel Mesh Electrodes: All electrodeposition processes were carried out in a standard three-electrode electrochemical cell with a 304 SS mesh or fluorine tin oxide (FTO)-coated glass substrates as the working electrode, a platinum mesh as the counter electrode, and Ag/AgCl/3.5 M KCl (0 V vs Ag/AgCl = 0.2 V vs SHE) as the reference electrode.

Prior to every electrodeposition, SS mesh was first ultrasonicated in 0.5 M H_2SO_4 solution for 10 min, rinsed subsequently with water, and then dried in air. The electrodeposition was conducted in 50 mL

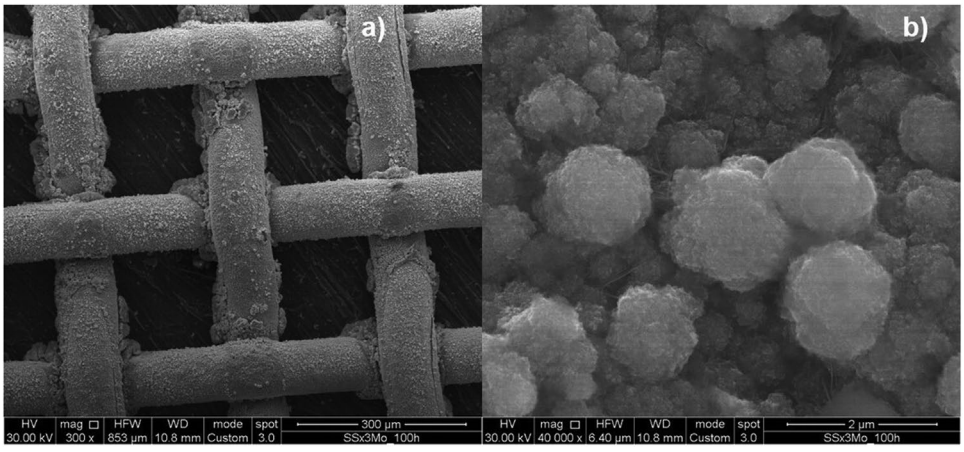

Figure 7. SEM images of 3Mo electrode at: a) low magnification and at: b) high magnification after 100 h stability test carried out at 100 mA cm^{-2}.

of aqueous solution containing 0.5 M $NiSO_4$, 12.5 mM $CuSO_4$, 0.5 M H_3BO_3, and different concentration of $(NH_4)_6Mo_7O_{24}$. The pH of the solution was corrected to 2.5 adding H_2SO_4. Aqueous solutions for the electrodeposition of pure Ni, Cu and Mo samples and of CuMo and NiMo samples contained the same concentration of Ni^{2+}, Cu^{2+} and MoO_4^{2-} ions. The electrodeposition was carried out with a VERSASTAT 3 workstation at –2.0 V vs Ag/AgCl for 600 s at room temperature.

Electrochemical Measurements: All electrochemical measurements were carried out with a PARSTAT 2263 workstation in a flow-through cell. The as-prepared electrode on 304 SS mesh was directly used as the working electrode without any further treatments. The exposed surface area of the steel mesh electrode was 0.5 cm^2. A dimensionally stable anode (DSA) and Hg/HgO/1 M NaOH were used as the counter electrode and reference electrode, respectively. All potentials measured were then referred to the reversible hydrogen electrode (RHE) using the following equation:

$$E_{RHE} = E_{Hg/HgO} + 0.1\,V + 0.059\,pH \quad (8)$$

EIS spectra were carried out at 0.15 V RHE in the case of estimating double layer capacitance (in a N_2 atmosphere) and at –0.15 V RHE in the frequency range of 0.1–10^5 Hz with an a.c. signal amplitude of 10 mV in 1 M KOH electrolyte by using PARSTAT 2263 workstation. EIS spectra were then fitted with ZSimpWin software with a suitable equivalent electrical circuit, described in the Results and Discussion section.

Galvanodynamic tests were carried out with a scan rate 1 mA cm^{-2} s^{-1} between –1 and –100 mA cm^{-2}. Stability tests were carried out as chronopotentiometric measurement at –100 mA cm^{-2} for 100 h.

Morphological and Structural Characterization: The specimens were examined by scanning electron microscopy (SEM) using a FEI Quanta 200 FEG SEM instrument at several magnifications, combined with a X-ray energy dispersive system (EDX).

X-ray diffraction (XRD) patterns for FTO after electrodeposition were recorded at room temperature on a PANalytical Empyrean diffractometer equipped with a PIXcel1D (tm) detector using the Cu$K\alpha$ radiation. A Ni filter was mounted at the exit of the X-ray source. In order to achieve, we used the highest signal-to-noise ratio, the operating conditions were 40 V and 40 mA.

XPS Characterization: X-ray photoelectron spectroscopy (XPS) analysis was carried out using a PHI5000 VersaProbe II scanning microprobe (ULVAC-PHI), operating with a monochromatic Al Kα source and X-Ray beam of 100 µm diameter. A take-off angle of the emitted photoelectrons of 45° relative to the surface was used. Peaks fitting was performed with MultiPak 9.9.2 (ULVAC-PHI), using Gauss–Loretz model and a Shirley-type background.

ICP-OES Test: For ICP–OES tests, all chemicals used were of analytical grade (Sigma Aldrich). To estimate metal release in solution, a calibration procedure was carried out with 0 (ultrapure water), 2, 5, 10, 20, 50, 100, 200, and 500 ppb for Ni, Cu, and Mo standard solutions. PerkinElmer Inc.-Optima 2100 DV was used for ICP–OES analysis. Samplings were carried out at the beginning of stability test, then after 25, 50, 75 h and at the end of test.

Supporting Information

Supporting Information is available from the Wiley Online Library or from the author.

Acknowledgements

Open Access Funding provided by Universita degli Studi di Palermo within the CRUI-CARE Agreement.

Conflict of Interest

The authors declare no conflict of interest.

Data Availability Statement

The data that support the findings of this study are available from the corresponding author upon reasonable request.

Keywords

alkaline electrolyzers, electrocatalysis, hydrogen evolution, porous transport layers, Pt-free electrocatalysts

Received: November 22, 2022
Revised: January 9, 2023
Published online: February 24, 2023

[1] S. R. Sinsel, R. L. Riemke, V. H. Hoffmann, *Renew. Energy* **2020**, *145*, 2271.
[2] M. Jafari, A. Botterud, A. Sakti, *Renewable Sustainable Energy Rev.* **2022**, *158*, 112077.
[3] S. Wu, N. Salmon, M. M. J. Li, R. Bañares-Alcántara, S. C. E. Tsang, *ACS Energy Lett.* **2022**, *7*, 1021.
[4] International Renewable Energy Agency (IRENA), *Green Hydrogen Cost Reduction: Scaling up Electrolysers to Meet the 1.5°C Climate Goal*, XX, Abu Dhabi **2020**.
[5] H. Nazir, C. Louis, S. Jose, J. Prakash, N. Muthuswamy, M. E. M. Buan, C. Flox, S. Chavan, X. Shi, P. Kauranen, T. Kallio, G. Maia, K. Tammeveski, N. Lymperopoulos, E. Carcadea, E. Veziroglu, A. Iranzo, A. M. Kannan, *Int. J. Hydrogen Energy* **2020**, *45*, 13777.
[6] X. Li, L. Zhao, J. Yu, X. Liu, X. Zhang, H. Liu, W. Zhou, *Nano-Micro Lett.* **2020**, *12*, 131.
[7] J. Zhang, Y. Zhao, X. Guo, C. Chen, C. L. Dong, R. S. Liu, C. P. Han, Y. Li, Y. Gogotsi, G. Wang, *Nat. Catal.* **2018**, *1*, 985.
[8] S. Chandrasekaran, L. Yao, L. Deng, C. Bowen, Y. Zhang, S. Chen, Z. Lin, F. Peng, P. Zhang, *Chem. Soc. Rev.* **2019**, *48*, 4178.
[9] European Commission, *Critical Materials for Strategic Technologies and Sectors in the EU – a Foresight Study*, Publications Office of the European Union, Luxembourg **2020**.
[10] R. Phillips, C. W. Dunnill, *RSC Adv.* **2016**, *6*, 100643.
[11] V. Vij, S. Sultan, A. M. Harzandi, A. Meena, J. N. Tiwari, W. G. Lee, T. Yoon, K. S. Kim, *ACS Catal.* **2017**, *7*, 7196.
[12] Z. W. She, J. Kibsgaard, C. F. Dickens, I. Chorkendorff, J. K. Nørskov, T. F. Jaramillo, *Science* **2017**, *355*, 146.
[13] J. Zhu, L. Hu, P. Zhao, L. Y. S. Lee, K. Y. Wong, *Chem. Rev.* **2020**, *120*, 851.
[14] J. R. McKone, B. F. Sadtler, C. A. Werlang, N. S. Lewis, H. B. Gray, *ACS Catal.* **2013**, *3*, 166.
[15] M. Wang, Z. Wang, X. Yu, Z. Guo, *Int. J. Hydrogen Energy* **2015**, *40*, 2173.
[16] M. Gong, W. Zhou, M. C. Tsai, J. Zhou, M. Guan, M. C. Lin, B. Zhang, Y. Hu, D. Y. Wang, J. Yang, S. J. Pennycook, B. J. Hwang, H. Dai, *Nat. Commun.* **2014**, *5*, 4695.
[17] C. Tang, L. Gan, R. Zhang, W. Lu, X. Jiang, A. M. Asiri, X. Sun, J. Wang, L. Chen, *Nano Lett.* **2016**, *16*, 6617.
[18] L. Yu, T. Lei, B. Nan, Y. Jiang, Y. He, C. T. Liu, *Energy* **2016**, *97*, 498.
[19] L. Wei, K. Goh, Ö. Birer, H. E. Karahan, J. Chang, S. Zhai, X. Chen, Y. Chen, *Nanoscale* **2017**, *9*, 4401.

[20] Q. Sun, Y. Dong, Z. Wang, S. Yin, C. Zhao, *Small* **2018**, *14*, 1704137.
[21] M. Pourbaix, *Atlas of Electrochemical Equilibria in Aqueous Solutions*, Pergamon Press, Oxford, UK **1966**.
[22] B. Hirschorn, M. E. Orazem, B. Tribollet, V. Vivier, I. Frateur, M. Musiani, *Electrochim. Acta* **2010**, *55*, 6218.
[23] Y. Li, X. Tan, R. K. Hocking, X. Bo, H. Ren, B. Johannessen, S. C. Smith, C. Zhao, *Nat. Commun.* **2020**, *11*, 2720.
[24] U. Sarac, R. M. Öksüzoğlu, M. C. Baykul, *J. Mater. Sci.* **2012**, *23*, 2110.
[25] S. H. Ahn, H. Y. Park, I. Choi, S. J. Yoo, S. J. Hwang, H. J. Kim, E. Cho, C. W. Yoon, H. Park, H. Son, J. M. Hernandez, S. W. Nam, T. H. Lim, S. K. Kim, J. H. Jang, *Int. J. Hydrogen Energy* **2013**, *38*, 13493.
[26] B. Hüner, N. Demir, M. F. Kaya, *Int. J. Hydrogen Energy* **2022**, *47*, 12136.
[27] H. You, P. Yang, X. Wang, X. Yang, Y. Sun, M. An, *J. Alloys Compd.* **2022**, *924*, 166407.
[28] A. Kim, N. Muthuchamy, C. Yoon, S. H. Joo, K. H. Park, *Nanomaterials* **2018**, *8*, 138.
[29] P. Cornette, S. Zanna, A. Seyeux, D. Costa, P. Marcus, *Corros. Sci.* **2020**, *174*, 108837.
[30] W. Kautek, J. G. Gordon, *J. Electrochem. Soc.* **1990**, *137*, 2672.
[31] Z. Wang, F. Di-Franco, A. Seyeux, S. Zanna, V. Maurice, P. Marcus, *J. Electrochem. Soc.* **2019**, *166*, C3376.
[32] Z. Wang, C. Carrière, A. Seyeux, S. Zanna, D. Mercier, P. Marcus, *Appl. Surf. Sci.* **2022**, *576*, 151836.
[33] M. Santamaria, F. Di Franco, F. Di Quarto, M. Pisarek, S. Zanna, P. Marcus, *J. Solid State Electrochem.* **2015**, *19*, 3511.
[34] M. Lao, P. Li, Y. Jiang, H. Pan, S. X. Dou, W. Sun, *Nano Energy* **2022**, *98*, 107231.
[35] Y. Pan, Y. Lin, Y. Liu, C. Liu, *Catal. Sci. Technol.* **2016**, *6*, 1611.
[36] S. Dong, Y. Li, Z. Zhao, R. Li, J. He, J. Yin, B. Yan, X. Zhang, *ChemistrySelect* **2022**, *7*, 202104041.
[37] Q. Quan, X. Bu, D. Chen, F. Wang, X. Kang, W. Wang, Y. Meng, S. Yip, C. Liu, J. C. Ho, *J. Mater. Chem. A Mater.* **2022**, *10*, 3953.
[38] J. Sun, B. Yu, F. Tan, W. Yang, G. Cheng, Z. Zhang, *Int. J. Hydrogen Energy* **2022**, *47*, 15764.
[39] R. Xiang, X. Wang, *ChemElectroChem* **2022**, *9*, 202200029.